

Bright and dark singlet excitons via linear and two-photon spectroscopy in monolayer transition-metal dichalcogenides

Timothy C. Berkelbach,¹ Mark S. Hybertsen,² and David R. Reichman³

¹*Princeton Center for Theoretical Science, Princeton University, Princeton, NJ 08544, USA*

²*Center for Functional Nanomaterials, Brookhaven National Laboratory, Upton, NY 11973-5000, USA*

³*Department of Chemistry, Columbia University, New York, NY 10027, USA*

We discuss the linear and two-photon spectroscopic selection rules for spin-singlet excitons in monolayer transition-metal dichalcogenides. Our microscopic formalism combines a fully k -dependent few-orbital band structure with a many-body Bethe-Salpeter equation treatment of the electron-hole interaction, using a model dielectric function. We show analytically and numerically that the single-particle, valley-dependent selection rules are preserved in the presence of excitonic effects. Furthermore, we definitively demonstrate that the bright (one-photon allowed) excitons have s -type azimuthal symmetry and that dark p -type excitons can be probed via two-photon spectroscopy. The screened Coulomb interaction in these materials substantially deviates from the $1/\epsilon_0 r$ form; this breaks the “accidental” angular momentum degeneracy in the exciton spectrum, such that the $2p$ exciton has a lower energy than the $2s$ exciton by at least 50 meV. We compare our calculated two-photon absorption spectra to recent experimental measurements.

I. INTRODUCTION

The transition-metal dichalcogenides (TMDCs) are a family of layered semiconducting crystals that includes MoS₂, MoSe₂, WS₂, and WSe₂. Isolated monolayers of TMDCs have been recently investigated for two major reasons. First, the emergent direct band-gap occurs at the corners of the hexagonal Brillouin zone (so-called ‘valleys’) [1, 2] and the nearby band structure topology leads to valley-dependent optical selection rules [3–5]. Second, the carrier confinement and reduced dielectric screening leads to large many-body effects, such as the formation of strongly bound excitons [6–10], trions [6, 11–13], and biexcitons [14] with very large binding energies. A unified understanding of the optical properties must treat both of these aspects on equal footing, and significant effort is now being focused on investigating the detailed spectroscopy of excitons in monolayer TMDCs.

In the ongoing effort to understand excitons in these materials, multiple spectroscopic techniques have been employed, including reflectance [9, 10, 15], photoluminescence excitation spectroscopy [16] scanning tunneling spectroscopy [17, 18], and two-photon luminescence [9, 19, 20]. A rigorous knowledge of the spectroscopic selection rules for excitons in monolayer TMDCs is crucial for the proper interpretation of these and future experiments. In this paper, we develop a model-based framework which is sufficiently detailed to provide quantitative results, but also sufficiently simple to allow precise statements about symmetry-determined selection rules. We describe the connection to our previous work based on an effective mass theory of excitons [6], and identify the key microscopic physical factors that determine the properties of excitons and their interaction with photons. We also provide the first theoretical treatment of two-photon absorption in monolayer TMDCs.

The outline of the paper is as follows. In Sec. II we will discuss simple microscopic models of the single-particle band structure in monolayer TMDCs, and in particular we will analyze the transition matrix elements which *completely* determine the independent-electron absorption and *partially* deter-

mine the excitonic absorption. We will then in Sec. III analyze the linear optical properties and present selection rules, both in the absence and presence of exciton effects, definitively finding that s -type excitons are optically bright. Lastly, in Sec. IV we will calculate the two-photon absorption signal which will be shown to probe p -type excitons and we will discuss some of the implications for recent experiments. We conclude in Sec. V, and make connection to other recent theoretical works. We note that a preliminary version of this work appeared in Ref. [21].

II. SINGLE-PARTICLE BAND STRUCTURE

We will consider two models for the single-particle band structure. First, we will consider a widely used long-wavelength, two-band model [3]. In particular, this minimal model allows for a largely analytical treatment, which exposes many of the subtleties of the theory, including selection rules and exciton effects. Second, we will use a recently presented nonlinear three-band model [22], which requires a numerical treatment but captures higher-order effects. This also ensures that our conclusions are generally valid and not specifically dependent on the simplified two-band picture. For simplicity we will henceforth neglect spin-orbit coupling, though it can be straightforwardly included in the single-particle description [3, 22, 23]. Specifically, in all models of the band structure, the spin projection s_z is still a good quantum number in the presence of spin-orbit coupling. In this sense, the following discussion applies to the A -exciton (and not the B -exciton) and conventional factors of two for spin will not appear. At this level of theory, the formalism for the B -exciton is identical, and its contribution is simply shifted to higher energies.

A. Two-band model

The first model considered has the form of a conventional two-band, massive Dirac Hamiltonian,

$$H_\tau(\mathbf{k}) = \begin{pmatrix} E_g/2 & at(\tau q_x - iq_y) \\ at(\tau q_x + iq_y) & -E_g/2 \end{pmatrix}. \quad (1)$$

The variable $\tau = \pm 1$ indexes the two “valleys,” known as the K and K' (or K and $-K$) points, which occur at alternating corners of the hexagonal first Brillouin zone. The Hamiltonian has been linearized in the wavevector difference with respect to the nearest K point, i.e. $\mathbf{q} = \mathbf{k} - \mathbf{K}$. This is a gapped version of the conventional graphene Hamiltonian [24]. In graphene, the spinor basis corresponds to carbon p_z orbitals on the two distinct sublattices; in the TMDCs, the basis corresponds to the transition-metal $|d_{z^2}\rangle \equiv |\phi_c\rangle$ orbital and the metal symmetry-adapted $|d_{x^2-y^2}\rangle + i\tau|d_{xy}\rangle \equiv |\phi_v^\tau\rangle$ orbital. The above Hamiltonian was first used for TMDCs by Xiao et al. [3] who predicted optical selection rules leading to spin-valley coupling. Such spin-valley coupling was quickly confirmed experimentally, by monitoring the circular polarization of photoluminescence [4, 5].

The eigenvalues of the two-band Hamiltonian are

$$E_{c/v}(\mathbf{k}) = \pm \frac{1}{2} \sqrt{E_g^2 + 4(atq)^2} \equiv \pm \varepsilon(\mathbf{k}) \quad (2)$$

and the eigenvectors are

$$|\psi_{c,\mathbf{k}}^\tau\rangle = \frac{1}{\sqrt{2}} \left[\sqrt{\alpha_+(\mathbf{k})} |\phi_c\rangle + \sqrt{\alpha_-(\mathbf{k})} e^{i\tau\phi_{\mathbf{k}}} |\phi_v^\tau\rangle \right] \quad (3a)$$

$$|\psi_{v,\mathbf{k}}^\tau\rangle = \frac{1}{\sqrt{2}} \left[-\sqrt{\alpha_-(\mathbf{k})} |\phi_c\rangle + \sqrt{\alpha_+(\mathbf{k})} e^{i\tau\phi_{\mathbf{k}}} |\phi_v^\tau\rangle \right]. \quad (3b)$$

where $\alpha_\pm(\mathbf{k}) = 1 \pm E_g/[2\varepsilon(\mathbf{k})]$ and $\tan \phi_{\mathbf{k}} = q_y/q_x$. The *relative* phase appearing within each eigenvector is associated with an electronic “chirality” (related to Berry’s phase), which is well-known in graphene [24–26]. Note that the *overall* phase of each eigenvector is arbitrary, and the phase convention chosen here is such that the first element of each eigenvector is purely real.

B. Three-band model

A more detailed Hamiltonian – using three bands derived from the transition-metal $|d_{z^2}\rangle$, $|d_{xy}\rangle$, and $|d_{x^2-y^2}\rangle$ atomic orbitals – was given recently by Liu et al [22]. The form of the matrix elements and material-specific parameters can be found in Ref. [22]. We note that in addition to using three bands instead of two, this Hamiltonian has *not* been linearized with respect to wavevector near the K and K' points, which gives a more accurate description throughout the entire Brillouin zone. While it cannot be so easily diagonalized analytically, the Hamiltonian can be straightforwardly diagonalized numerically. For phase consistency in later calculations, we enforce the same phase convention as for the two-band eigenvectors, i.e. that the first element of each eigenvector is purely

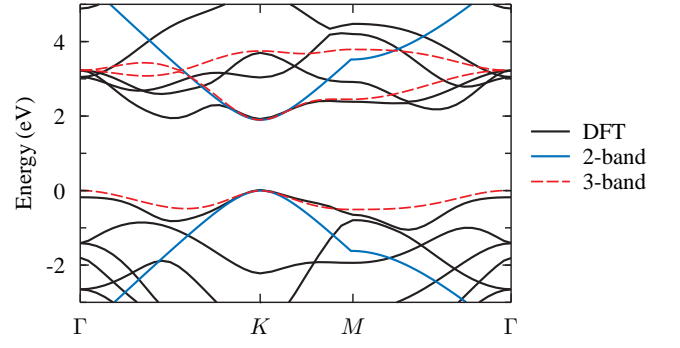


FIG. 1. Single-particle band structure of MoS₂ predicted by a linearized two-band model (blue solid) and a non-linear three-band model (red dashed) compared to first-principles density functional theory with the local density approximation (DFT, solid black).

real, which is sufficient to ensure continuity in k -space. In Fig. 1, the band structure predicted by these two models is compared to the band structure calculated by density functional theory with the local density approximation.

C. Transition matrix elements

An analysis of optical selection rules requires the momentum matrix elements between single-particle states. In the present model Hamiltonians, the momentum matrix elements normal to the layer are zero by symmetry. Here we focus on the momentum in the plane. By using the commutation relation $\mathbf{p} = (-im/\hbar)[\mathbf{r}, H]$, we can write these momentum matrix elements as

$$\begin{aligned} \mathbf{P}^{vc}(\mathbf{k}) &= \frac{-im}{\hbar} \langle \psi_{v,\mathbf{k}} | [\mathbf{r}, H] | \psi_{c,\mathbf{k}} \rangle \\ &= \frac{m}{\hbar} (E_{c,\mathbf{k}} - E_{v,\mathbf{k}}) \langle \psi_{v,\mathbf{k}} | \nabla_{\mathbf{k}} | \psi_{c,\mathbf{k}} \rangle \end{aligned} \quad (4)$$

where we have used the k -space representation of the position operator, $\mathbf{r} = i\nabla_{\mathbf{k}}$. We can now use a generalized Feynman-Hellman theorem to write this as

$$\mathbf{P}^{vc}(\mathbf{k}) = \frac{m}{\hbar} \langle \psi_{v,\mathbf{k}} | \nabla_{\mathbf{k}} H(\mathbf{k}) | \psi_{c,\mathbf{k}} \rangle \quad (5)$$

(note that this expression neglects the on-site, intra-atomic contribution [27], however this vanishes here for $d-d$ transitions). For the simple two-band Hamiltonian, this gives

$$\nabla_{\mathbf{k}} H(\mathbf{k}) = \begin{pmatrix} 0 & at(\tau \hat{x} - i\hat{y}) \\ at(\tau \hat{x} + i\hat{y}) & 0 \end{pmatrix}. \quad (6)$$

The appropriate matrix element can then be taken between the conduction and valence band eigenstates of the Hamiltonian, yielding a transition dipole vector $\mathbf{P}^{vc}(\mathbf{k})$ with linear x - and y -polarization components

$$P_x^{vc}(\mathbf{k}) = \tau \frac{mat}{2\hbar} [\alpha_+(\mathbf{k}) e^{-i\tau\phi_{\mathbf{k}}} - \alpha_-(\mathbf{k}) e^{i\tau\phi_{\mathbf{k}}}], \quad (7)$$

$$P_y^{vc}(\mathbf{k}) = i \frac{mat}{2\hbar} [\alpha_+(\mathbf{k}) e^{-i\tau\phi_{\mathbf{k}}} + \alpha_-(\mathbf{k}) e^{i\tau\phi_{\mathbf{k}}}]. \quad (8)$$

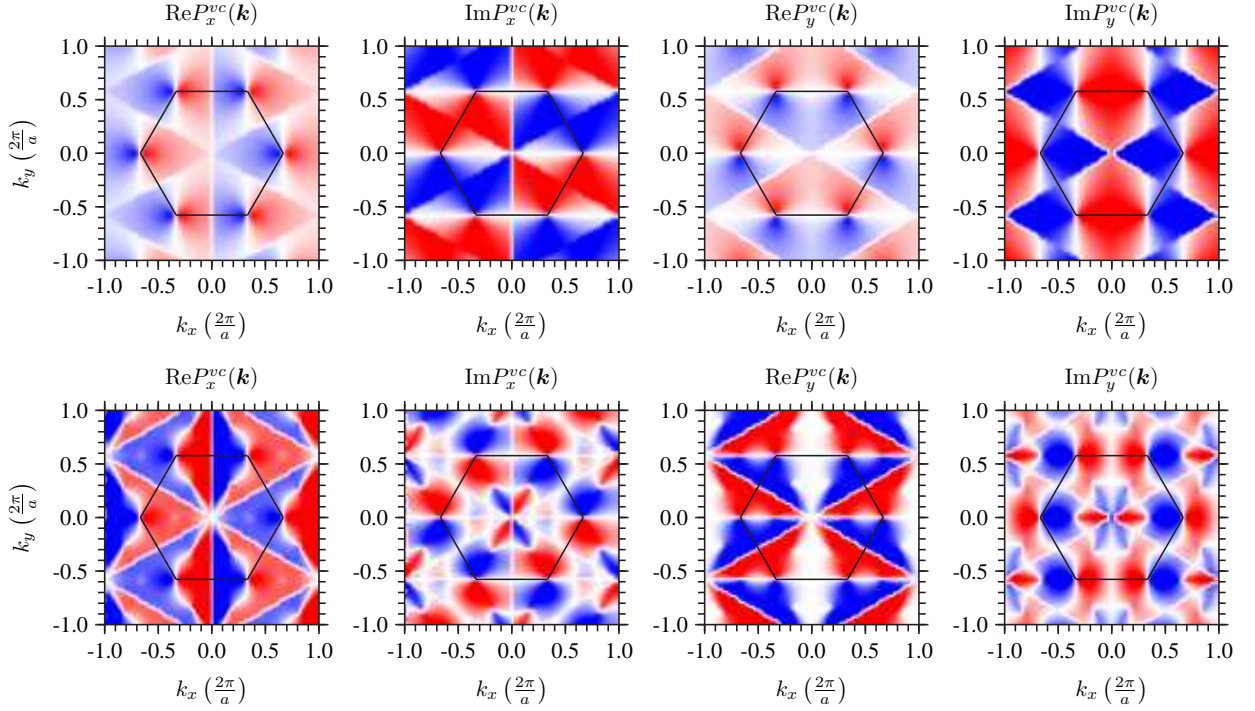


FIG. 2. Valence to lowest conduction band momentum matrix elements for a linearized two-band model (top) and a non-linear three-band model (bottom). Blue is positive, red is negative, and white is zero. The results are qualitatively very similar in the immediate vicinity of the K and K' points, but differ elsewhere in the Brillouin zone.

The same procedure can be done for the three-band Hamiltonian, by taking the gradient and calculating (numerically) the appropriate matrix element between conduction and valence bands. A comparison of the real and imaginary parts of the x - and y -components of the two different models of the band structure is shown in Fig. 2 throughout the entire first Brillouin zone.

Valley-dependent selection rules have been shown to arise specifically for the case of circularly polarized light [3]. For circular polarizations, the above expressions can be combined to give, in the two-band case,

$$P_{\pm}^{vc}(\mathbf{k}) = \frac{1}{\sqrt{2}} \left[P_x^{vc}(\mathbf{k}) \pm iP_y^{vc}(\mathbf{k}) \right] \\ = \mp \frac{mat}{\sqrt{2}\hbar} \left(1 \mp \tau \frac{E_g}{2\varepsilon(\mathbf{k})} \right) e^{\pm i\phi_{\mathbf{k}}}, \quad (9)$$

leading to the valley-dependent intensities,

$$|P_{\pm}^{vc}(\mathbf{k})|^2 = \frac{m^2 a^2 t^2}{2\hbar^2} \left(1 \mp \tau \frac{E_g}{2\varepsilon(\mathbf{k})} \right)^2. \quad (10)$$

Near the K and K' points, $2\varepsilon(\mathbf{k}) \rightarrow E_g$, such that $P_{\pm}^{vc}(\mathbf{k}) \propto (1 \mp \tau)e^{\pm i\phi_{\mathbf{k}}}$ and $|P_{\pm}^{vc}(\mathbf{k})|^2 \propto (1 \mp \tau)^2$, i.e. circular polarization can selectively excite electrons at the K or K' point. For example, right-handed circular polarization, $P_{-}^{vc}(\mathbf{k})$, selectively excites at the K ($\tau = +1$) point. Again, this analysis can be carried out numerically for the three-band model. A comparison of the the selection rules, $|P_{\pm}^{vc}(\mathbf{k})|^2$, for the two models is

shown in Fig. 3. Note that while the matrix elements themselves have an ambiguity in the phase (i.e. they are not observable), the squared matrix elements are completely independent of the phase convention. In Sec. III B, we will show how the nodal structure (p -type symmetry) of the momentum matrix elements is canceled, leading to bright s -type excitons which still respect the valley selectivity.

III. LINEAR OPTICAL PROPERTIES AND SELECTION RULES

In general, the transition probability per unit time is given by

$$W(\omega) = \frac{2\pi}{\hbar} \sum_F |V_{IF}|^2 \delta(E_F - E_I - \hbar\omega) \quad (11)$$

where V_{IF} is the matrix element which couples the initial and final states with energies E_I and E_F . For the linear (one-photon) absorption, we have $V = (eA/mc)\boldsymbol{\lambda} \cdot \hat{\mathbf{p}}$, where A is the vector potential and $\boldsymbol{\lambda}$ is the polarization. Within the presently considered model Hamiltonians, symmetry excludes coupling to photons with electric vector polarized perpendicular to the plane of the monolayer. Here we explicitly consider the case with electric vector polarized in the plane. We will evaluate this expression first in the independent particle picture and then in the presence of excitonic effects.

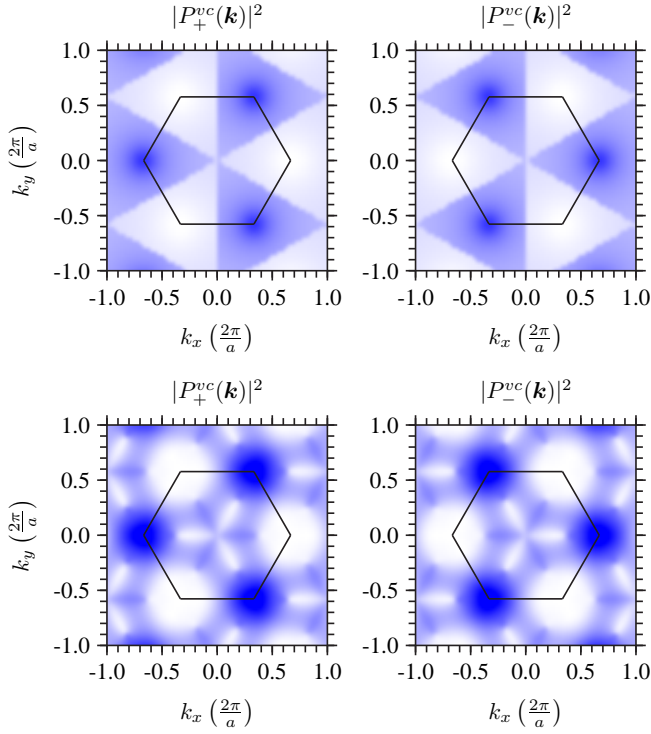


FIG. 3. Valence to lowest conduction band momentum matrix elements squared, for circular polarization, for a linearized two-band model (top) and a non-linear three-band model (bottom). Black is positive and white is zero. The results are qualitatively very similar in the immediate vicinity of the K and K' points, but differ elsewhere in the Brillouin zone.

A. Independent particle absorption

For an uncorrelated initial ground state $|0\rangle$ and an uncorrelated final excited state $c_{c,\mathbf{k}}^\dagger c_{v,\mathbf{k}}|0\rangle$, it is simple to show

$$V_{IF} = \frac{eA}{mc} \langle 0 | \boldsymbol{\lambda} \cdot \hat{\mathbf{p}} c_{c,\mathbf{k}}^\dagger c_{v,\mathbf{k}} | 0 \rangle = \frac{eA}{mc} \boldsymbol{\lambda} \cdot \mathbf{P}^{vc}(\mathbf{k}), \quad (12)$$

$$E_F - E_I = E_c(\mathbf{k}) - E_v(\mathbf{k}), \quad (13)$$

and therefore

$$W(\omega) = \frac{2\pi}{\hbar} \left(\frac{eA}{mc} \right)^2 \sum_{cv,\mathbf{k}} |\boldsymbol{\lambda} \cdot \mathbf{P}^{vc}(\mathbf{k})|^2 \times \delta(E_c(\mathbf{k}) - E_v(\mathbf{k}) - \hbar\omega). \quad (14)$$

The imaginary part of the dielectric function [28] follows as [29]

$$\varepsilon_2(\omega) = \frac{4\pi^2 e^2}{m^2 \omega^2} \sum_{cv} \int_{BZ} \frac{d^2 k}{(2\pi)^2} |\boldsymbol{\lambda} \cdot \mathbf{P}^{vc}(\mathbf{k})|^2 \times \delta(E_c(\mathbf{k}) - E_v(\mathbf{k}) - \hbar\omega), \quad (15)$$

where we have taken the infinite-system limit. Let us specifically consider the linearized two-band model with right-handed circular polarization, $\boldsymbol{\lambda} \cdot \mathbf{P}^{vc}(\mathbf{k}) = P_-^{vc}(\mathbf{k})$, for which

we can carry out the integration in Eq. (15) semi-analytically. Considering only one valley (say $\tau = +1$), we can change to polar coordinates about the K point,

$$\varepsilon_2^K(\omega) = \frac{2\pi e^2}{m^2 \omega^2} \int_0^\infty k |P_-^{vc}(k)|^2 \delta(2\varepsilon(k) - \hbar\omega) dk. \quad (16)$$

Note that by integrating out to infinity, we are incurring an error at large wavevectors (energies). Since the dispersion relation is monotonic, we can change variables, $kdk = \varepsilon d\varepsilon / a^2 t^2$, and use the squared matrix element from above to find

$$\begin{aligned} \varepsilon_2^K(\omega) &= \frac{\pi e^2}{\hbar^2 \omega^2} \int_0^\infty d\varepsilon \theta(2\varepsilon - E_g) \varepsilon \left(1 + \frac{E_g}{2\varepsilon} \right)^2 \delta(2\varepsilon - \hbar\omega) \\ &= \frac{\pi e^2}{4\hbar\omega} \theta(\hbar\omega - E_g) \left(1 + \frac{E_g}{\hbar\omega} \right)^2. \end{aligned} \quad (17)$$

Accounting for the other valley, $\varepsilon_2(\omega) = \varepsilon_2^K(\omega) + \varepsilon_2^{K'}(\omega)$, yields

$$\begin{aligned} \varepsilon_2(\omega) &= \frac{\pi e^2}{4\hbar\omega} \theta(\hbar\omega - E_g) \left[\left(1 + \frac{E_g}{\hbar\omega} \right)^2 + \left(1 - \frac{E_g}{\hbar\omega} \right)^2 \right] \\ &= \frac{\pi e^2}{2\hbar\omega} \theta(\hbar\omega - E_g) \left(1 + \frac{E_g^2}{(\hbar\omega)^2} \right). \end{aligned} \quad (18)$$

At energies just above the gap, the dielectric function is like that of a conventional 2D semiconductor, i.e. $\omega^2 \varepsilon_2(\omega) = \text{const}$, but at higher energies it behaves like graphene (due to the linear dispersion), i.e. $\omega \varepsilon_2(\omega) = \text{const}$. However, the linear dispersion is unrealistic for TMDCs, as can be seen in the full band structure (Fig. 1).

B. Exciton absorption and the Bethe-Salpeter equation

We now consider the spin-singlet optical properties including the excitonic effects arising from the strong electron-hole interaction. The *correlated* excited states within the single-excitation approximation can be written as

$$|X\rangle = \sum_{\mathbf{k}} \sum_{vc} A_{vc}^X(\mathbf{k}) c_{c,\mathbf{k}}^\dagger c_{v,\mathbf{k}} |0\rangle, \quad (19)$$

where $|0\rangle$ is again an uncorrelated (determinantal) ground state. This form for the excited state wavefunction underlies the time-dependent Hartree-Fock and Bethe-Salpeter equation (BSE) formalisms; here we will pursue the latter, which is a many-body perturbative theory in the screened two-particle interaction. For a periodic crystal exciton wavefunction, Eq. (19), the BSE is an eigenvalue problem [30] for the exciton energy E_X ,

$$E_X A_{vc}^X(\mathbf{k}) = (E_{c,\mathbf{k}} - E_{v,\mathbf{k}}) A_{vc}^X(\mathbf{k}) + \frac{1}{A} \sum_{\mathbf{k}'} \sum_{v',c'}^{BZ} \langle \psi_{v,\mathbf{k}} \psi_{c,\mathbf{k}} | K^{eh} | \psi_{v',\mathbf{k}'} \psi_{c',\mathbf{k}'} \rangle A_{v'c'}^X(\mathbf{k}'). \quad (20)$$

The electron-hole interaction kernel K^{eh} is the sum of a frequency-dependent screened Coulomb interaction and an unscreened exchange interaction [30],

$$\langle \psi_{v,\mathbf{k}} \psi_{c,\mathbf{k}} | K^{eh,d} | \psi_{v',\mathbf{k}'} \psi_{c',\mathbf{k}'} \rangle = - \int d^d \mathbf{r} \int d^d \mathbf{r}' \psi_{c,\mathbf{k}}^*(\mathbf{r}) \psi_{c',\mathbf{k}'}(\mathbf{r}) W(\mathbf{r}, \mathbf{r}', \omega) \psi_{v,\mathbf{k}}(\mathbf{r}') \psi_{v',\mathbf{k}'}^*(\mathbf{r}') \quad (21a)$$

$$\langle \psi_{v,\mathbf{k}} \psi_{c,\mathbf{k}} | K^{eh,x} | \psi_{v',\mathbf{k}'} \psi_{c',\mathbf{k}'} \rangle = \int d^d \mathbf{r} \int d^d \mathbf{r}' \psi_{c,\mathbf{k}}^*(\mathbf{r}) \psi_{v,\mathbf{k}}(\mathbf{r}) |\mathbf{r} - \mathbf{r}'|^{-1} \psi_{c',\mathbf{k}'}(\mathbf{r}') \psi_{v',\mathbf{k}'}^*(\mathbf{r}'). \quad (21b)$$

If we (i) neglect the exchange interaction, (ii) neglect the frequency-dependence and local-field effects of the screened direct interaction, i.e. $W(\mathbf{r}, \mathbf{r}', \omega) \approx W(\mathbf{r} - \mathbf{r}', \omega = 0)$, and (iii) make a ‘zero differential overlap’ approximation for the atomic orbitals, we find

$$\langle \psi_{v,\mathbf{k}} \psi_{c,\mathbf{k}} | K^{eh} | \psi_{v',\mathbf{k}'} \psi_{c',\mathbf{k}'} \rangle \approx - \langle \psi_{c,\mathbf{k}} | \psi_{c',\mathbf{k}'} \rangle \langle \psi_{v',\mathbf{k}'} | \psi_{v,\mathbf{k}} \rangle W(\mathbf{k} - \mathbf{k}'). \quad (22)$$

In the above, we have neglected the possible orbital structure to the screened interaction $W_{ij}(\mathbf{r} - \mathbf{r}')$.

At this point, we wish to emphasize that the orbital overlap prefactor in the screened interaction is crucially important. As an explicit example, in the two-band picture, we have

$$\langle \psi_{c,\mathbf{k}}^\tau | \psi_{c,\mathbf{k}'}^\tau \rangle = \frac{1}{2} \left[\sqrt{\alpha_+(\mathbf{k}) \alpha_+(\mathbf{k}')} + \sqrt{\alpha_-(\mathbf{k}) \alpha_-(\mathbf{k}')} e^{-i\tau(\phi_{\mathbf{k}} - \phi_{\mathbf{k}'})} \right], \quad (23a)$$

$$\langle \psi_{v,\mathbf{k}'}^\tau | \psi_{v,\mathbf{k}}^\tau \rangle = \frac{1}{2} \left[\sqrt{\alpha_-(\mathbf{k}') \alpha_-(\mathbf{k})} + \sqrt{\alpha_+(\mathbf{k}') \alpha_+(\mathbf{k})} e^{i\tau(\phi_{\mathbf{k}} - \phi_{\mathbf{k}'})} \right]. \quad (23b)$$

As before, near the K and K' points, $2\varepsilon(\mathbf{k}) \rightarrow E_g$, [i.e. $\alpha_+(\mathbf{k}) \approx 1$ and $\alpha_-(\mathbf{k}) \approx 0$], and in this limit,

$$\langle \psi_{c,\mathbf{k}}^\tau | \psi_{c,\mathbf{k}'}^\tau \rangle \approx 1 \quad (24a)$$

$$\langle \psi_{v,\mathbf{k}'}^\tau | \psi_{v,\mathbf{k}}^\tau \rangle \approx e^{i\tau(\phi_{\mathbf{k}} - \phi_{\mathbf{k}'})}. \quad (24b)$$

The BSE, Eq. (20), then yields a Wannier-like, two-band picture with an unusual phase factor in the screened interaction,

$$E_X A_{vc}^X(\mathbf{k}) = (E_{c,\mathbf{k}} - E_{v,\mathbf{k}}) A_{vc}^X(\mathbf{k}) - \frac{1}{A} \sum_{\mathbf{k}'}^{BZ} W(\mathbf{k} - \mathbf{k}') e^{i\tau(\phi_{\mathbf{k}} - \phi_{\mathbf{k}'})} A_{vc}^X(\mathbf{k}'). \quad (25)$$

Multiplying through by $e^{-i\tau\phi_{\mathbf{k}}}$ gives a conventional Wannier equation for the pseudo-wavefunction $\tilde{A}_{vc}^X(\mathbf{k}) = e^{-i\tau\phi_{\mathbf{k}}} A_{vc}^X(\mathbf{k})$. If the bands can be approximated as parabolic, this means that the energy *spectrum* of the BSE is identical to that of a corresponding real-space Wannier equation with a screened interaction $W(\mathbf{r})$, as we have employed in previous work [6, 10],

$$[E_X - E_g] \tilde{A}_{vc}^X(\mathbf{r}) = \left[-\frac{1}{2\mu} \nabla_{\mathbf{r}}^2 - W(\mathbf{r}) \right] \tilde{A}_{vc}^X(\mathbf{r}) \quad (26)$$

However, as explained in a recent work by Srivastava and Imamoglu [31], systematically continuing the expansion of Eqs. (24) for small $\mathbf{k} - \mathbf{k}'$ leads to additional terms in the

Coulomb interaction that weakly break certain degeneracies (see below). In this case, the spectrum of Eqs. (25) and (26) is no longer identical to that of the BSE with the screened interaction given in Eq. (22).

It remains to be shown whether the exciton wavefunctions of the original problem, as described by the BSE (25), have the same selection rules or the same spatial symmetries as the wavefunction of the real-space Wannier equation (26). To analyze the spatial symmetries, we can calculate the real-space wavefunction corresponding to the solution of the BSE, with the hole position fixed at the origin. We find

$$\begin{aligned} \Psi_X(\mathbf{r}_e, \mathbf{r}_h = 0) &\equiv \sum_{\mathbf{k}} A_{vc}^X(\mathbf{k}) \psi_{c,\mathbf{k}}(\mathbf{r}_e) \psi_{v,\mathbf{k}}^*(0) \\ &\approx \sum_{\mathbf{k}} A_{vc}^X(\mathbf{k}) e^{-i\tau\phi_{\mathbf{k}}} e^{i\mathbf{k} \cdot \mathbf{r}_e} = \tilde{A}_{vc}^X(\mathbf{r}_e), \end{aligned} \quad (27)$$

demonstrating that the wavefunction which solves the real-space Eq. (26) is indeed (approximately) the same as the real-space BSE wavefunction. At a less approximate level, the spatial *symmetries* (s , p , d , etc.) will be identical. This is one of the main conclusions of this work.

To determine the selection rules, we now consider the optical absorption in the presence of correlated excitonic effects. Assuming as before an uncorrelated initial (ground) state $|I\rangle = |0\rangle$, but now using a Wannier-like final exciton state $|X\rangle$ as in Eq. (19) gives

$$\langle I | \lambda \cdot \hat{\mathbf{p}} | X \rangle = \sum_{\mathbf{k}} A_{vc}^X(\mathbf{k}) \lambda \cdot \mathbf{P}^{vc}(\mathbf{k}), \quad (28)$$

which leads to the dielectric function

$$\varepsilon_2(\omega) = \frac{4\pi^2 e^2}{m^2 \omega^2} \sum_X \left| \sum_{\mathbf{k}} A_{vc}^X(\mathbf{k}) \lambda \cdot \mathbf{P}^{vc}(\mathbf{k}) \right|^2 \delta(\hbar\omega - E_X). \quad (29)$$

Recall that for right-handed circular polarization, the momentum matrix element near the K' ($\tau = -1$) point is nearly zero

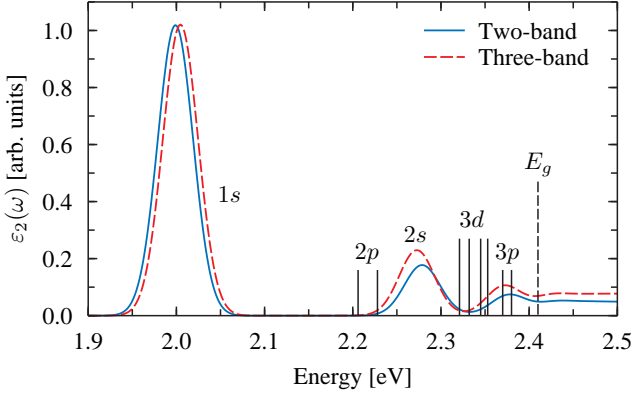


FIG. 4. Imaginary part of the dielectric function for MoS₂ calculated in the presence of excitonic effects. The band gap has been rigidly increased to 2.41 eV such that the 1s exciton peak occurs near 2.0 eV (spin-orbit splitting into A and B peaks is neglected, as described in the text). A Gaussian broadening of 50 meV (FWHM) has been applied to all peaks.

and near the K ($\tau = 1$) point it is given by

$$\lambda \cdot P^{vc}(\mathbf{k}) = P_{-}^{vc}(\mathbf{k}) \approx \frac{\sqrt{2}mat}{\hbar} e^{-i\phi_{\mathbf{k}}} \equiv P_0 e^{-i\phi_{\mathbf{k}}}. \quad (30)$$

Therefore we can restrict our attention to \mathbf{k} near K , which gives

$$\langle I | \lambda \cdot \hat{\mathbf{p}} | X \rangle = P_0 \sum_{\mathbf{k} \sim K} A_{vc}^X(\mathbf{k}) e^{-i\phi_{\mathbf{k}}} = P_0 \tilde{A}_{vc}^X(\mathbf{r} = 0) \quad (31)$$

and therefore

$$\varepsilon_2(\omega) = \frac{4\pi e^2 P_0^2}{m^2 \omega^2} \sum_X |\tilde{A}_{vc}(\mathbf{r} = 0)|^2 \delta(\hbar\omega - E_X), \quad (32)$$

which is just the usual Elliott formula for the excitonic absorption [32]. In particular, the selection rules are conventional in that they are determined by the behavior of the wavefunction at the origin in real-space, leading to bright states with s -type azimuthal symmetry. We emphasize that the phase factor appearing in the momentum matrix element is essentially cancelled by the conjugate phase factor in the exciton envelope wavefunction, which itself originates from the change of basis in the screened interaction, Eq. (22). Therefore, not only can the excitons be labeled in analogy with the hydrogen series in terms of their spatial symmetries but, to lowest order, they also obey identical selection rules. This is the second main conclusion of this work.

As usual, the same analysis cannot be done analytically on the three-band model, but it can be straightforwardly carried out numerically. The dielectric function calculated via Eq. (29) for the two considered band structure models of MoS₂ is plotted in Fig. 4; in particular, the orbital overlaps in Eq. (22) are calculated numerically, without the approximation given in Eqs. (24). As described in Refs. [6, 10], the screened interaction used in the calculations is given by

$$W(\mathbf{k}) = \frac{2\pi e^2}{k(1 + 2\pi\chi_{2D}k)} \quad (33)$$

with $\chi_{2D} = 6.6 \text{ \AA}$ for intrinsic MoS₂. Results are presented for a 120×120 sampling of the Brillouin zone, which we have found necessary to converge the binding energy to roughly 0.1 eV accuracy, in agreement with the fully *ab initio* BSE study presented in Ref. [7]. Specifically, for MoS₂ this sampling gives a 1s exciton binding energy of 0.41 eV, however an extrapolation to the infinite sampling limit gives approximately 0.52 eV, in good agreement with our prior result obtained in Ref. [6] (0.54 eV). In Fig. 4, the conduction bands have been rigidly shifted to increase the band gap to 2.41 eV, such that the 1s exciton peak occurs near its experimentally observed value of 2.0 eV (due to the spin-orbit interaction, this peak is actually split into the so-called A and B peaks at about 1.9 and 2.0 eV respectively [2]). An important conclusion to be drawn from Fig. 4 is that the more realistic band structure generates only minor quantitative differences in $\varepsilon_2(\omega)$, compared to that generated by the two band model.

The labeling of states in Fig. 4 is done via inspection of the wavefunction, in either reciprocal or real-space. For example, in Fig. 5 we show the selection-rule-determining product $A_{vc}^X(\mathbf{k})P_{-}^{vc}(\mathbf{k})$ [which is closely related to the pseudo-wavefunction $\tilde{A}_{vc}^X(\mathbf{k})$] for right-handed polarization. The symmetries of the exciton wavefunctions are apparent, and the valley selectivity is also recovered in the presence of excitonic effects.

Focusing on the features in the $\varepsilon_2(\omega)$ spectrum that derive from the s -type exciton states, the Rydberg series is nonhydrogenic, as discussed in detail in Refs. [10, 16]. This follows from the unusual form of the screened Coulomb interaction for these monolayer thick materials. In particular, it deviates substantially from the $1/\varepsilon_0 r$ form that dominates in conventional semiconductors. The Hamiltonian with this latter interaction has additional symmetry which leads to the “accidental” angular momentum degeneracy in the hydrogen spectrum. Here that symmetry is broken: we find that for a given principal quantum number, the larger angular momentum states are more strongly bound, i.e. $E_{1s} < E_{2p} < E_{2s} < E_{3d}$ and so on. The same behavior has been recently observed in a fully *ab initio* BSE calculation [19], and the present work provides a simple physical explanation for this behavior in terms of the effective screened interaction (see also Refs. [33, 34] for similar findings). To verify this unconventional disposition of dark exciton states requires a nonlinear spectroscopic measurement, which we discuss in the next section. Furthermore, we also note a small splitting of the $2p$, $3d$, and $3p$ dark exciton states. In particular, the 20 meV splitting of the $2p$ states is in good agreement with recent results [31, 33]. As mentioned before, Srivastava and Imamoglu have traced this degeneracy breaking to the orbital overlaps in Eq. (22) and explained the effect in terms of Berry curvature in the single-particle band structure [31].

IV. TWO-PHOTON ABSORPTION

Our theoretical framework for the two-photon absorption essentially follows the early work of Mahan [35] for 3D semiconductors and Shimizu [36] for 2D quantum wells including

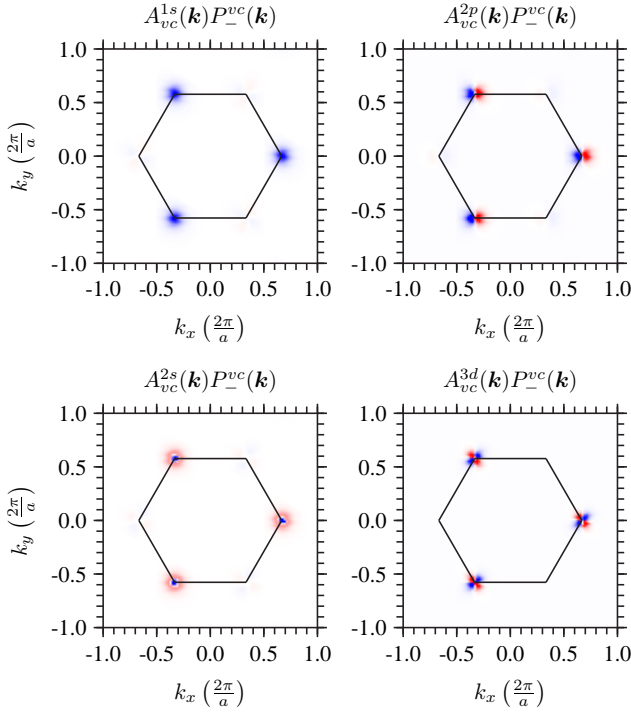


FIG. 5. Reciprocal space plots of the selection-rule-determining product $A_{vc}^X(\mathbf{k})P_{-}^{vc}(\mathbf{k})$. In the presence of right-handed circular polarization, it is seen that excitons are only created at the K point, and not at the K' point, as was found in Ref. [3] and in Sec. IIC in the *absence* of exciton effects.

explicit consideration of excitons. For a two-photon process, the transition rate is again given by Eq. (11), except we now have two perturbing fields, $V_i = (eA_i/mc)\lambda_i \cdot \hat{\mathbf{p}}$ ($i = 1, 2$), where A_i is the vector potential, λ_i is the polarization, and $\hbar\omega_i$ is the photon energy. The matrix element of the perturbation can be evaluated by a sum over intermediate states $|M\rangle$,

$$V_{IF} = \left(\frac{e}{mc}\right)^2 A_1 A_2 \sum_M \left[\frac{\langle I|\lambda_2 \cdot \hat{\mathbf{p}}|M\rangle \langle M|\lambda_1 \cdot \hat{\mathbf{p}}|F\rangle}{E_M - E_I - \hbar\omega_1} + \frac{\langle I|\lambda_1 \cdot \hat{\mathbf{p}}|M\rangle \langle M|\lambda_2 \cdot \hat{\mathbf{p}}|F\rangle}{E_M - E_I - \hbar\omega_2} \right]. \quad (34)$$

The two-photon spectroscopy of single-particle states is trivial, and so we restrict our analysis to the excitonic case. As in the one-photon exciton absorption, Eq. (31) holds for the matrix element connecting the ground and *intermediate* exciton states. In contrast, the matrix element between two exciton states (intermediate and final) is

$$\begin{aligned} \langle M|\lambda_1 \cdot \hat{\mathbf{p}}|F\rangle &= \hbar \sum_{\mathbf{k}} A_{vc}^{M*}(\mathbf{k}) \lambda_1 \cdot \mathbf{k} A_{vc}^F(\mathbf{k}) \\ &= \hbar \sum_{\mathbf{k}} \tilde{A}_{vc}^{M*}(\mathbf{k}) e^{-i\tau\phi_{\mathbf{k}}} \lambda_1 \cdot \mathbf{k} \tilde{A}_{vc}^F(\mathbf{k}) e^{i\tau\phi_{\mathbf{k}}} \\ &= -i\hbar \int d^2r \tilde{A}_{vc}^{M*}(\mathbf{r}) \lambda_1 \cdot \nabla_{\mathbf{r}} \tilde{A}_{vc}^F(\mathbf{r}). \end{aligned} \quad (35)$$

In the above, we have restricted the analysis to two bands (c, v) and used the facts that the expectation value of $\hat{\mathbf{p}}$ is zero in a

Slater determinant and that $\hat{\mathbf{p}}$ is diagonal in reciprocal space. To have a nonzero Eq. (35) requires that the real-space exciton wavefunctions A^F and A^M have orbital angular momenta which differ by ± 1 ; this is the same two-photon selection rule as found in conventional semiconductors including consideration of exciton effects. Combined with the result of the previous section – that one-photon absorption produces s -type excitons – we conclude that two-photon absorption produces only p -type excitons. With these results, the two-photon absorption essentially follows the early work of Mahan [35] for 3D semiconductors or Shimizu [36] for 2D quantum wells.

The primary complication in the evaluation of two-photon absorption is the evaluation of the internal sum over intermediate states in Eq. (34). We follow the approximation introduced by Mahan [35] and used by Shimizu [36] that allows the sum to be eliminated with a completeness relation. Explicitly incorporating the above results, the first term in Eq. (34) can be written as (the second term is analogous)

$$\begin{aligned} -i\hbar P_0 \int d^2r \sum_M \frac{\tilde{A}_{vc}^M(\mathbf{r}=0) \tilde{A}_{vc}^{M*}(\mathbf{r})}{E_M - E_I - \hbar\omega_1} \lambda_1 \cdot \nabla_{\mathbf{r}} \tilde{A}_{vc}^F(\mathbf{r}) \\ \approx \frac{-i\hbar P_0}{E_g - \langle E_b \rangle - \hbar\omega_1} \left[\lambda_1 \cdot \nabla_{\mathbf{r}} \tilde{A}_{vc}^F(\mathbf{r}) \right]_{\mathbf{r}=0} \end{aligned} \quad (36)$$

where $\langle E_b \rangle$ is an average intermediate (s -type) exciton energy introduced to facilitate the (complete) sum over intermediate states; for simplicity we will henceforth set $\langle E_b \rangle$ to zero as its primary influence is to simply alter the prefactor. In contrast to the hydrogenic exciton case, where further results can be obtained analytically, the matrix elements here must be evaluated numerically.

The two-photon transition rate is thus given by

$$\begin{aligned} W(\Omega) &= 2\pi\hbar \left(\frac{e}{mc}\right)^4 (A_1 A_2)^2 (\hbar P_0)^2 \\ &\times \sum_F \left| \frac{\left[\lambda_1 \cdot \nabla_{\mathbf{r}} \tilde{A}_{vc}^F(\mathbf{r}) \right]_{\mathbf{r}=0}}{E_g - \hbar\omega_1} + \{1 \leftrightarrow 2\} \right|^2 \delta(\hbar\Omega - E_F) \end{aligned} \quad (37)$$

where $\hbar\Omega = \hbar\omega_1 + \hbar\omega_2$. The simplest case to consider is when $\lambda_1 = \lambda_2$ and $\hbar\omega_1 = \hbar\omega_2 \approx E_g/2$, which gives

$$W(\Omega) = W_0 \sum_F \left| \lambda \cdot \nabla_{\mathbf{r}} \tilde{A}_{vc}^F(\mathbf{r}) \right|_{\mathbf{r}=0}^2 \delta(\hbar\Omega - E_F) \quad (38)$$

where

$$W_0 = \frac{32\pi\hbar^3 e^4 A_1^2 A_2^2 P_0^2}{m^4 c^4 E_g^2}. \quad (39)$$

If both photons have the same circular polarization, then this experiment probes valley-selective p -type excitons, which are dark in the linear measurement. Using photons with opposite polarizations would create p -type excitons in both valleys.

Motivated by recent nonlinear spectroscopic measurements on WSe₂ [9] and WS₂ [19], in Fig. 6 we show the results of a numerical evaluation of Eq. (38) for these two materials; the exciton wavefunctions and their derivatives have been

obtained from the real-space effective mass treatment of the two-band model (i.e. the small splitting of the p excitons is neglected). The agreement with experiment, for both the linear and nonlinear response, is seen to be quite good. In the calculations, we have used the same screening length, $\chi_{2D} = 7.0$ Å for both materials, which yields an exciton binding energy of 0.48 eV (in accord with our previous results [6]). We note that this exciton binding energy is slightly larger than that determined in Refs. [9, 10] (0.37 and 0.32 eV for WSe₂ and WS₂ respectively).

In the narrow linewidth limit, the two-photon absorption identifies the p -type excitons with energies slightly below that of the corresponding s -type exciton. For a larger linewidth, the $2p$ transition is still resolved and responsible for the main peak seen in experiment, while the remaining transitions merge to yield a weak feature before the continuum onset. Importantly, ratio between the $2p$ peak height and the higher-energy signal (near the continuum onset) is determined by the spectral linewidth. It is thus encouraging that our simulated spectrum simultaneously reproduces the $2p$ linewidth and this intensity ratio; the required broadening suggests that it should be difficult to observe the $3p$ transition at this resolution. This leaves open the origin of the small feature observed near 2.5 eV in the experimental spectrum for WS₂.

Finally, we point out that a recent study on WSe₂ using one- and two-photon photoluminescence excitation spectroscopy [20], has identified the $2s$ and $2p$ transitions to have the same energy to meV accuracy. This is in quite stark contrast with the results of the present work, which suggest that the $2p$ exciton should be lower in energy by *at least* 50 meV. We hope that future work, both experimental and theoretical, is devoted to investigating this discrepancy.

V. CONCLUSIONS

In this work, we have expanded the effective mass theory presented in Refs. [6, 10] to include a fully k -dependent model of the band structure, in harmony with other recent works [8, 33, 37]. This extension allows for deviations from parabolicity, including trigonal warping behavior which has been emphasized in other contexts [23, 38]. We find that two- and three-band models of the single-particle band structure give nearly identical results for the exciton properties within a simplified BSE formalism, suggesting that trigonal warping is a secondary effect. Furthermore, our numerical results are nearly identical to those of the effective mass treatment from our previous work [6, 10], justifying its use in those contexts. We have definitively proved that spin-singlet excitons with s -type azimuthal symmetry, which have been the most studied [6, 8, 10], are indeed the optically bright excitons. As in our previous work [10, 16], we confirm that the disposition of bright exciton states is distinctly non-hydrogenic.

The dark spin-singlet excitons have also been investigated and found to exhibit another deviation from the hydrogen model, in the form of a broken angular momentum degeneracy. Using an approach similar to ours, the authors of Refs. [33, 34] have identified the same qualitative behavior.

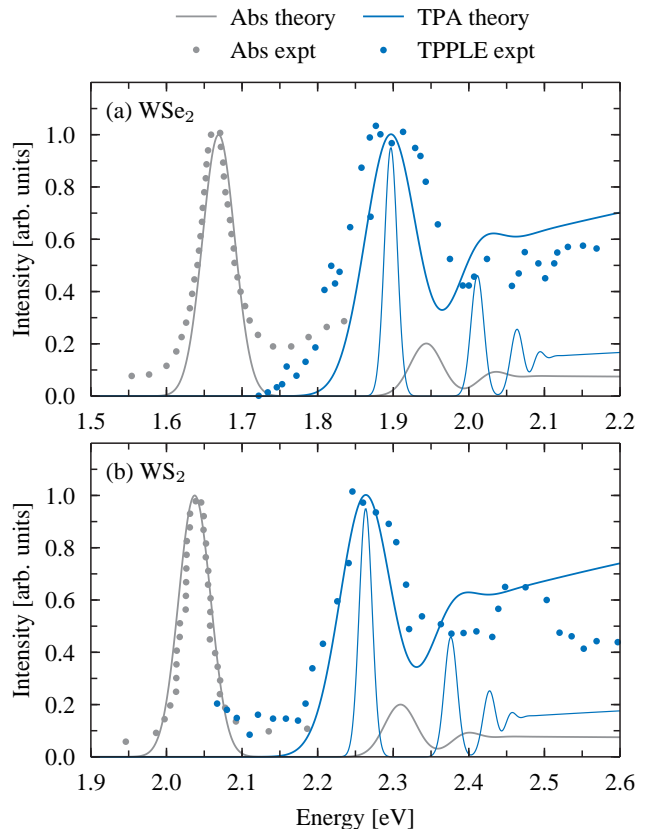


FIG. 6. Two-photon absorption (TPA) intensity for monolayer (a) WSe₂ and (b) WS₂ evaluated numerically with Eq. (38) (blue lines). The spectra have been artificially broadened with a Gaussian linewidth (FWHM) of 80 meV (thicker line) and 20 meV (thinner line). The experimental two-photon photoluminescence excitation (TPPLE) spectrum for WSe₂ [9] and WS₂ [19] is included for comparison (blue circles). The theoretical linear absorption spectrum from the same model (FWHM of 50 meV) is overlaid for reference (grey lines) along with the experimental result (grey circles) for WSe₂ [9] and WS₂ [15].

This observation will be key in future analyses of two-photon spectroscopies on TMDCs. A recent manuscript contains results from a fully *ab initio* BSE calculation on WS₂ and also finds this peculiar angular momentum behavior [19]. It is clearly encouraging that our simple low-energy theory – featuring a few-band representation of the single-particle states and an appropriate treatment of screening with a model dielectric function – is able to correctly reproduce the optical selection rules, the character of bright and dark exciton states, the broken angular momentum degeneracy, the quantitatively large exciton binding energies, and the spectral features of the nonlinear two-photon absorption. In this regard, we believe the model presented here represents perhaps the simplest predictive minimal model capable of unifying these wide-ranging features in monolayer TMDCs.

Note added. As discussed in the main text, a recent preprint analyzes the impact of the band overlap factors in the effective Coulomb interaction, Eq. (22), and systematically develops the next order terms in $k - k'$, demonstrating signatures of the

Berry curvature in the exciton spectra [31]. Our numerical results agree with their analysis and with their estimate for the splitting of the $2p$ exciton levels. Figure 4 was updated to reflect these splittings.

ACKNOWLEDGMENTS

The authors would like to thank Alexey Chernikov and Tony F. Heinz for invaluable discussions. T.C.B thanks Ajit Srivastava for informative correspondence regarding Ref. [31]. Part of this work was supported by the Princeton Center for Theoretical Science (TCB), and part of this work was done using resources of the Center for Functional Nanomaterials, which is a U.S. DOE Office of Science User Facility, at Brookhaven National Laboratory under Contract No. DE-SC0012704 (MSH).

-
- [1] A. Splendiani, L. Sun, Y. Zhang, T. Li, J. Kim, C.-Y. Chim, G. Galli, and F. Wang, *Nano Lett.* **10**, 1271 (2010).
 - [2] K. F. Mak, C. Lee, J. Hone, J. Shan, and T. F. Heinz, *Phys. Rev. Lett.* **105**, 136805 (2010).
 - [3] D. Xiao, G.-B. Liu, W. Feng, X. Xu, and W. Yao, *Phys. Rev. Lett.* **108**, 196802 (2012).
 - [4] H. Zeng, J. Dai, W. Yao, D. Xiao, and X. Cui, *Nature Nanotech.* **7**, 490 (2012).
 - [5] K. F. Mak, K. He, J. Shan, and T. F. Heinz, *Nature Nanotech.* **7**, 494 (2012).
 - [6] T. C. Berkelbach, M. S. Hybertsen, and D. R. Reichman, *Phys. Rev. B* **88**, 045318 (2013).
 - [7] D. Y. Qiu, F. H. da Jornada, and S. G. Louie, *Phys. Rev. Lett.* **111**, 216805 (2013).
 - [8] G. Berghäuser and E. Malic, *Phys. Rev. B* **89**, 125309 (2014).
 - [9] K. He, N. Kumar, L. Zhao, Z. Wang, K.-F. Mak, H. Zhao, and J. Shan, *Phys. Rev. Lett.* **113**, 026803 (2014).
 - [10] A. Chernikov, T. C. Berkelbach, H. M. Hill, A. Rigosi, Y. Li, Ö. B. Aslan, D. R. Reichman, M. S. Hybertsen, and T. F. Heinz, *Phys. Rev. Lett.* **113**, 076802 (2014).
 - [11] K. F. Mak, K. He, C. Lee, G.-H. Lee, J. Hone, T. F. Heinz, and J. Shan, *Nature Mater.* **12**, 207 (2013).
 - [12] J. S. Ross, S. Wu, H. Yu, N. J. Ghimire, A. M. Jones, G. Aivazian, J. Yan, D. G. Mandrus, D. Xiao, W. Yao, and X. Xu, *Nature Comm.* **4**, 1474 (2013).
 - [13] A. M. Jones, H. Yu, N. J. Ghimire, S. Wu, G. Aivazian, J. S. Ross, B. Zhao, J. Yan, D. G. Mandrus, D. Xiao, W. Yao, and X. Xu, *Nature Nanotech.* **8**, 634 (2013).
 - [14] Y. You, X.-X. Zhang, T. C. Berkelbach, M. S. Hybertsen, D. R. Reichman, and T. F. Heinz, *Nature Phys.* **11**, 477 (2015).
 - [15] Y. Li, A. Chernikov, X. Zhang, A. Rigosi, H. M. Hill, A. M. van der Zande, D. A. Chenet, E.-M. Shih, J. Hone, and T. F. Heinz, *Phys. Rev. B* **90**, 205422 (2014).
 - [16] H. M. Hill, A. F. Rigosi, C. Roquelet, A. Chernikov, T. C. Berkelbach, D. R. Reichman, M. S. Hybertsen, L. E. Brus, and T. F. Heinz, *Nano Lett.* **15**, 2992 (2015).
 - [17] C. Zhang, A. Johnson, C.-L. Hsu, L.-J. Li, and S.-K. Shih, *Nano Lett.* **14**, 2443 (2014).
 - [18] M. M. Ugeda, A. J. Bradley, S.-F. Shi, F. H. da Jornada, Y. Zhang, D. Y. Qiu, W. Ruan, S.-K. Mo, Z. Hussain, Z.-X. Shen, F. Wang, S. G. Louie, and M. F. Crommie, *Nature Mater.* **13**, 1091 (2014).
 - [19] Z. Ye, T. Cao, K. O'Brien, H. Zhu, X. Yin, Y. Wang, S. G. Louie, and X. Zhang, *Nature* **513**, 214 (2014).
 - [20] G. Wang, X. Marie, I. Gerber, T. Amand, D. Lagarde, L. Bouet, M. Vidal, A. Balocchi, and B. Urbaszek, *Phys. Rev. Lett.* **114**, 097403 (2015).
 - [21] T. C. Berkelbach, *Microscopic theories of excitons and their dynamics*, Ph.D. thesis, Columbia University (2014).
 - [22] G.-B. Liu, W.-Y. Shan, Y. Yao, W. Yao, and D. Xiao, *Phys. Rev. B* **88**, 085433 (2013).
 - [23] A. Kormányos, V. Zólyomi, N. D. Drummond, P. Rakyta, G. Burkard, and V. I. Fal'ko, *Phys. Rev. B* **88**, 045416 (2013).
 - [24] A. H. Castro Neto, F. Guinea, N. M. R. Peres, K. S. Novoselov, and A. K. Geim, *Rev. Mod. Phys.* **81**, 109 (2009).
 - [25] A. K. Geim and K. S. Novoselov, *Nature Mater.* **6**, 183 (2007).
 - [26] Y. Barlas, T. Pereg-Barnea, M. Polini, R. Asgari, and A. H. MacDonald, *Phys. Rev. Lett.* **98**, 236601 (2007).
 - [27] T. G. Pedersen, K. Pedersen, and T. B. Kriestensen, *Phys. Rev. B* **63**, 201101(R) (2001).
 - [28] Strictly, this is a 2D dielectric function, with units of length, akin to a sheet polarizability per unit area.
 - [29] F. Bassani and G. Pastori-Parravicini, *Electronic States and Optical Transitions in Solids* (Pergamon Press, New York., 1975).
 - [30] M. Rohlfing and S. G. Louie, *Phys. Rev. B* **62**, 4927 (2000).
 - [31] A. Srivastava and A. Imamoglu, [arXiv:1507.04040](https://arxiv.org/abs/1507.04040).
 - [32] R. J. Elliott, *Phys. Rev.* **108**, 1384 (1957).
 - [33] F. Wu, F. Qu, and A. H. MacDonald, *Phys. Rev. B* **91**, 075310 (2015).
 - [34] A. Chaves, T. Low, P. Avouris, D. Çakır, and F. M. Peeters, *Phys. Rev. B* **91**, 155311 (2015).
 - [35] G. D. Mahan, *Phys. Rev.* **170**, 825 (1968).
 - [36] A. Shimizu, *Phys. Rev. B* **40**, 1403 (1989).
 - [37] S. Konabe and S. Okada, *Phys. Rev. B* **90**, 155304 (2014).
 - [38] H. Rostami, A. G. Moghaddam, and R. Asgari, *Phys. Rev. B* **88**, 085440 (2013).